

Coupled Spin and Valley Hall Effects Driven by Coherent Tunneling

W. Zeng*

Department of physics, Jiangsu University, Zhenjiang 212013, China

We predict the coexistence of tunneling spin and valley Hall effects when electrons in graphene coherently transmit through a barrier with broken inversion symmetry and intrinsic spin-orbit coupling. Due to the rotation of the pseudospin in the tunneling process, the transmitted electrons acquire a finite spin- and valley-dependent backreflection geometric phase when the two interfaces of the barrier are asymmetric. This results in a spin- and valley-dependent skew coherent tunneling, which is responsible for the transverse spin and valley Hall currents. We further demonstrate that the coherent-tunneling assisted charge-spin and charge-valley conversions are highly efficient with large Hall angles. Our work provides a new route for the generation of efficient spin and valley Hall effects, suggesting potential applications for spintronic and valleytronic devices.

Introduction.—The possibility of using the spin and valley degrees of freedom to store and carry information leads to the emergence of spintronics and valleytronics [1–3], respectively, where the spin Hall effect (SHE) and valley Hall effect (VHE) have attracted much attention in recent years. Both SHE and VHE can be generated through either extrinsic or intrinsic mechanisms. The extrinsic SHE is attributed to the spin-dependent scattering of charge carriers by impurities in the presence of the spin-orbit coupling [4, 5], whereas the intrinsic SHE is absent of any scattering processes and stems from the spin-orbit coupling in the electronic band structure [6, 7]. The extrinsic VHE can be realized by breaking the time-reversal symmetry, such as through the extrinsic magnetism caused by the magnetic proximity effect [8] and the external light fields [9, 10]. The intrinsic VHE is directly linked to the band topology, and the Hall conductance is proportional to the integration over the Fermi sea of the Berry curvature of each occupied band [11, 12]. The coupled SHE and VHE have been proposed in monolayers of MoS₂ and other group-VI dichalcogenides [13], where the VHE, accompanied by a SHE, can be generated intrinsically by spin- and valley-dependent Berry curvature, or extrinsically by external optical fields. Recently, the valley-dependent SHE has been predicted in monolayer transition-metal dichalcogenides [14], where the valley-polarized spin currents and transverse spin accumulations can be generated by microwave irradiation.

Apart from the aforementioned methods, the skew tunneling in heterojunctions is an alternative mechanism to generate the SHE and VHE in the ballistic regime, which are termed as the *tunneling* Hall effects. The tunneling spin Hall effect (TSHE) has been reported in magnetic tunnel junctions with broken time-reversal symmetry [15–17] and the tunneling valley Hall effect (TVHE) has been predicted in the tunnel junctions with tilted Dirac cones [18, 19]. Both the existing TSHE and TVHE are associated with the momentum filtering and are independent of the Berry curvature.

In contrast to the previously predicted TSHE and TVHE, here we propose a tunneling Hall effect driven by the phase-coherent tunneling in graphene heterojunctions. Both the TSHE and TVHE can be generated without the need for breaking time-reversal symmetry or in the absence of tilted Dirac cones. Compared with the existing TSHE and TVHE, the

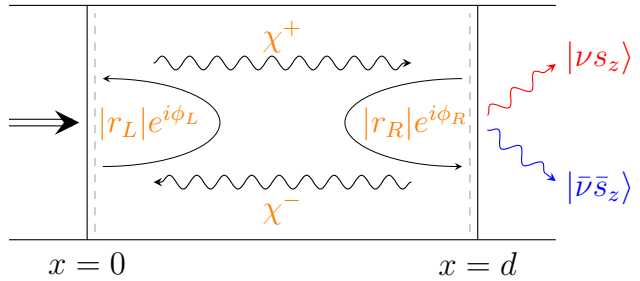


FIG. 1. Schematic of the tunneling process. The tunnel junction is divided into three parts. The left and right electrode regions are located at $x < 0$ and $x > d$, respectively. The barrier region is located at $0 < x < d$, where the right and left propagating states are denoted by χ^+ and χ^- , respectively. The backreflections occur at the left and right interfaces of the barrier with the reflection amplitudes being $|r_L|e^{i\phi_L}$ and $|r_R|e^{i\phi_R}$, respectively. The transmitted state with valley and spin indices $|v, s_z\rangle$ and its time-reversal counterpart $|\bar{v}\bar{s}_z\rangle$ ($\bar{v} = -v$, $\bar{s}_z = -s_z$) are denoted by the red and blue wavy lines, respectively.

physical origin of the predicted coherent-tunneling assisted Hall effect is attributed to the coherence of the tunneling acquired geometric phase rather than the time-reversal symmetry breaking induced momentum filtering [15–17] or the tilt-induced Fermi surface mismatch [18, 19]. In addition, the previously predicted TSHE and TVHE are independent of the Berry curvature, whereas the non- π Berry flux is essential in our model. We further demonstrate that the coherent-tunneling assisted charge-spin and charge-valley conversions are highly efficient with large Hall angles, suggesting potential applications for spintronic and valleytronic devices.

Model.—We consider the graphene-based tunnel junction in the $x - y$ plane, as shown in Fig. 1. The junction is divided into the left electrode region ($x < 0$), right electrode region ($x > d$), and the central barrier region ($0 < x < d$). In the barrier region, the pseudospin staggered potential and the intrinsic spin-orbit coupling are considered. Theoretical and experimental investigations demonstrate that the pseudospin staggered potential and the intrinsic spin-orbit coupling can be induced in graphene by the proximity effect of substrates such as transition metal dichalcogenides [20–23]. In the left

and right electrode regions, the electric transport property is described by the Dirac Hamiltonian [24]

$$\mathcal{H}_{L/R} = v_F(v p_x \sigma_x + p_y \sigma_y) - \mu_{L/R}, \quad (1)$$

where v_F is the Fermi velocity, $v = +(-)$ for K (K') valley, $p_{x,y} = -i\partial_{x,y}$ are the two-dimensional momenta in the $x - y$ plane (we set $\hbar = 1$), and $\sigma_{x,y}$ are the Pauli matrices in the sublattice space. $\mu_{L/R}$ is the Fermi energy in the left/right electrode regions, which can be adjusted by doping or by a gate voltage. In the barrier region, the Hamiltonian is given by [23, 25, 26]

$$\mathcal{H}_b = v_F(v p_x \sigma_x + p_y \sigma_y) - \mu_b + h_I, \quad (2)$$

$$h_I = \Delta \sigma_z + v s_z \lambda \sigma_0. \quad (3)$$

Here μ_b is the Fermi energy in the barrier region. h_I is the substrate interaction term consisting of the staggered potential ($\Delta \sigma_z$) and the intrinsic spin-orbit coupling ($v s_z \lambda \sigma_0$), which can be induced by the proximity effect of substrates in the barrier region. σ_z is the z -component of the Pauli matrix in the sublattice space and $s_z = +1$ (-1) for the up (down) spin of the electrons. The substrate interaction term breaks the inversion symmetry by the staggered potential $\Delta \sigma_z$ but preserves the time-reversal symmetry. Consequently, the state $|v s_z\rangle$ and its time-reversal counterpart $|\bar{v} \bar{s}_z\rangle$ ($\bar{v} = -v$, $\bar{s}_z = -s_z$) are degenerate with the energy dispersion $E = \pm \sqrt{(v_F|\mathbf{p}|)^2 + \Delta^2 + v s_z \lambda - \mu_b}$, where \pm for the conduction and valence bands, respectively. The energy dispersion implies that the intrinsic spin-orbit coupling leads to a Zeeman splitting of 2λ , which has opposite sign in the K and K' valleys and leads to an out-of-plane spin polarization with the opposite polarization in each valley.

The net transmission amplitude of the single-barrier tunneling can be expressed in a general Fabry-Pérot form [27, 28]

$$t = t_L t_R / (1 - |r_L r_R| e^{i\phi}), \quad (4)$$

where r_j ($j = L, R$) is the reflection amplitude for the j interface with its backreflection phase being $\phi_j = \arg(r_j)$; see Fig. 1. $\phi = \phi_L + \phi_R$ is the total backreflection phase acquired in the barrier region. t_j is the transmission amplitude, which satisfies $|t_j|^2 + |r_j|^2 = 1$ due to the current conservation.

The scattering amplitudes t_j , r_j ($j = L, R$) and the backreflection phase $\arg(r_j)$ can be readily obtained by matching the wave functions independently at the j interface of the tunnel junction. For the right interface at $x = d$, the scattering wave function can be described by

$$\psi_R(x) = \begin{cases} r_R \chi^- e^{-i p_b x} + \chi^+ e^{i p_b x}, & x < d, \\ t_R \tilde{\chi}^+ e^{i p_R x}, & x > d. \end{cases} \quad (5)$$

Here the spinors $\chi^\pm = (\kappa \cos \varphi_b)^{-1/2} (\kappa e^{\mp i v \varphi_b / 2}, \pm e^{\pm i v \varphi_b / 2})^T$ are the right and left propagating states in the barrier region, respectively; see Fig. 1. $\tilde{\chi}^+ = (\cos \varphi_R)^{-1/2} (e^{-i v \varphi_R / 2}, e^{i v \varphi_R / 2})^T$ is the transmitted state in the right electrode. p_b and p_R are the transmission angle in the barrier and right electrode regions,

respectively, with the corresponding transmission angles being φ_b and φ_R , which satisfy $\tan \varphi_{b(R)} = p_y / p_{b(R)}$ with p_y being the conserved transverse momentum labeling different trajectories. The spin- and valley-dependent parameter κ is given by

$$\kappa^2 = \frac{\zeta + \Delta}{\zeta - \Delta}, \quad (6)$$

where $\zeta = \epsilon + \mu_b - v s_z \lambda$ with ϵ being the incident energy. For the left interface at $x = 0$, the scattering states can be obtained simply by substituting $(\chi^\pm, \tilde{\chi}^+) \rightarrow (\chi^\mp, \tilde{\chi}^-)$ and $(t_R, r_R, p_R) \rightarrow (t_L, r_L, p_L)$ in Eq. (5). Here the spinor $\tilde{\chi}^- = (\cos \varphi_L)^{-1/2} (e^{i v \varphi_L / 2}, -e^{-i v \varphi_L / 2})^T$ is the left propagating basis state in the left electrode region with φ_L being the transmission angle satisfying $\sin \varphi_L = v_F p_y / (\epsilon + \mu_L)$.

Carefully invoking the boundary conditions at $x = 0$ and $x = d$ to determine r_j and t_j ($j = L, R$) yields the transmission probability

$$T_j = 4\kappa \cos \varphi_b \cos \varphi_j / (1 + \kappa^2 + 2\kappa \cos(\varphi_b + \varphi_j)). \quad (7)$$

The reflection probability is given by $R_j = 1 - T_j$ due to the current conservation.

The total backreflection phase can be directly obtained by $\phi = \arg(r_L) + \arg(r_R)$. One finds that ϕ can be divided into two parts, *i.e.*, $\phi = \phi_0 + \phi_G$, where

$$\phi_0 = 2p_b d \quad (8)$$

is the kinetic phase due to the motion of electrons in the barrier with $p_b = (\zeta^2 - \Delta^2 - v_F^2 p_y^2)^{-1/2}$ being the longitudinal momentum, and the additional phase ϕ_G is given by

$$\tan \phi_G = f_{v s_z} \times v \Delta (\mu_R - \mu_L) p_y. \quad (9)$$

Here the spin- and valley-dependent parameter $f_{v s_z}$ is an even function of p_y and satisfies $f_{v s_z} = f_{\bar{v} \bar{s}_z}$; see supplemental material for more details. ϕ_G is dependent on the junction parameters and disappears when either $\Delta = 0$ or $\mu_L = \mu_R$. In addition, distinct from the kinetic phase ϕ_0 , ϕ_G changes sign under the substitution $p_y \rightarrow -p_y$, namely

$$p_y \rightarrow -p_y \implies \begin{cases} \phi_0 \rightarrow \phi_0, \\ \phi_G \rightarrow -\phi_G. \end{cases} \quad (10)$$

The additional phase shift ϕ_G originates from the rotation of the pseudospin of the Dirac fermions in the reflection at the left and right interfaces of the barrier, which is termed as the geometric phase. Contrary to the usual Berry phase, the backreflection geometric phase can be acquired by the single electron tunneling process through the interfaces of the barrier, where the incident state, reflected state in the barrier and the transmitted state in the electrode can be mapped onto the Bloch sphere by the pseudospin polarization vectors. The acquired backreflection geometric phase at the left/right interface can be quantitatively written as $\phi_{G,L/R} = -\Omega_{L/R}/2$ [29, 30], where $\Omega_{L/R}$ is the solid angle covered by the geodesic triangle on Bloch sphere connecting the incident state, reflected

state, and the state orthogonal to the transmitted state at the left/right interface of the barrier. The total geometric phase can be obtained as $\phi_G = \phi_{G,L} + \phi_{G,R} = -(\Omega_L + \Omega_R)/2$. This acquired geometric phase can be electrically tuned by the junction control, leading to geometric-phase devices such as the topological waveguides and topological transistor [31].

To more quantitatively analyze the geometrical origin of ϕ_G , the pseudospin polarization vectors of the scattering states are obtained; see supplemental material for more details. The solid angle Ω_j ($j = L, R$) is covered by the the geodesic triangle on Bloch sphere connecting \mathbf{d}_+ , \mathbf{d}_- , and \mathbf{d}_j , where \mathbf{d}_\pm and \mathbf{d}_j are the pseudospin polarization vectors of the states in the barrier and the j electrode, respectively. One finds that \mathbf{d}_j always lies on the equator of the Bloch sphere, whereas the position of \mathbf{d}_\pm on the Bloch sphere is dependent on κ . Specifically, the z component of \mathbf{d}_\pm is given by $\Phi/\pi - 1$, where $\Phi = 2\pi\kappa^2/(1 + \kappa^2)$ is the spin- and valley-dependent Berry flux in the barrier region. When the inversion symmetry is preserved ($\Delta = 0$ and $\Phi = \pi$), both Ω_L and Ω_R disappear due to \mathbf{d}_\pm and \mathbf{d}_j lie on the equator of the Bloch sphere, indicating $\phi_G = 0$. In addition, when $\mu_L = \mu_R$, two symmetric interfaces of the barrier lead to $\Omega_L = -\Omega_R$, where ϕ_G is also absent.

Consequently, a nonzero ϕ_G requires two essential conditions: (i) inversion symmetry breaking ($\Delta \neq 0$), ensuring that both Ω_L and Ω_R are nonzero, and (ii) asymmetric barrier interfaces ($\mu_L \neq \mu_R$), ensuring that $\Omega_L \neq -\Omega_R$; see Eq. (9).

TSHE and TVHE.—The net transmission probability through the barrier can be obtained by squaring t in Eq. (4). With the help of Eqs. (7) and (10), we obtain

$$T(p_y) = \sum_n g_n \cos^n(\phi_0 + \phi_G), \quad (11)$$

$$T(-p_y) = \sum_n g_n \cos^n(\phi_0 - \phi_G), \quad (12)$$

where $g_n = T_L T_R (4R_L R_R)^{n/2} / (1 + R_L R_R)^{n+1}$ with $n \in \mathbb{N}$. Consequently, the nonzero ϕ_G yields $T(p_y) \neq T(-p_y)$, leading to a skew coherent tunneling. We note that the net transmission probabilities in Eqs. (11) and (12) are spin- and valley-dependent, namely $T(p_y) = T_{vs_z}(p_y)$, where the valley and spin indices ‘ v, s_z ’ are omitted here for simplicity.

The transmission probability as a function of the transverse momentum p_y is shown in Figs. (2)(a)-(2)(d). In our calculations, we take $\Delta = 3.25$ meV and $\lambda = 2.5$ meV, which are consistent with the *ab initio* calculations for the staggered potential and the intrinsic spin-orbit coupling in graphene induced by proximity to the transition metal dichalcogenide substrates, such as WS₂ [23]. For the given valley and spin indices, ϕ_G changes sign when p_y is reversed, leading to a large anisotropy for the p_y -resolved transmission probability; see Figs. (2)(a) and (2)(b). The transverse valley and spin imbalances occur due to $T_{vs_z}(p_y) \neq T_{\bar{v}s_z}(p_y)$ and $T_{vs_z}(p_y) \neq T_{v\bar{s}_z}(p_y)$, respectively, where $\bar{v} = -v$ and $\bar{s}_z = -s_z$. The net valley- and spin-dependent transmission probabilities (given by $T_v = \sum_{s_z} T_{vs_z}$ and $T_{s_z} = \sum_v T_{vs_z}$, respectively) are shown in Figs. (2)(c) and (2)(d). The valley-dependent transmission probability in

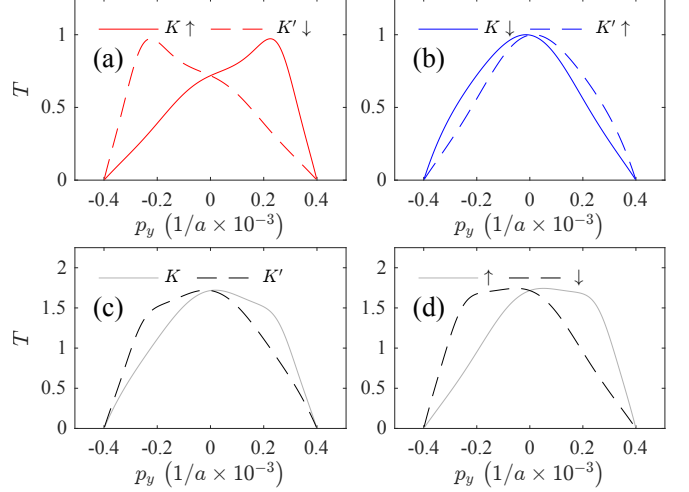


FIG. 2. Spin- and valley-resolved transmission probability versus the transverse momentum p_y (in units of $1/a \times 10^{-3}$ with a being the lattice constant of graphene). The parameters are $\epsilon = 1.8$ meV, $\Delta = 3.25$ meV, $\lambda = 2.5$ meV, $\mu_L = 1$ meV, $\mu_R = -5.6$ meV, $\mu_b = 6.5$ meV and $d = 25$ nm. (a) Transmission probability for the state $|K\uparrow\rangle$ and its time-reversal counterpart $|K'\downarrow\rangle$. (b) Transmission probability for the state $|K\downarrow\rangle$ and its time-reversal counterpart $|K'\uparrow\rangle$. (c) Transmission probability for electrons from different valleys. (d) Transmission probability for electrons with different spins.

Fig. (2)(c) indicates that the electrons in K valley have a large transmission for the incident angles in the range of 0° to 90° , whereas the transmissions in K' valley are similarly asymmetric but skewed into the opposite direction, leading to the electrons with opposite valleys turning into different transverse directions, which is responsible for the net transverse valley currents. Similarly, the net transverse spin currents also occur due to the skew behaviors of T_{s_z} , as shown in Fig. 2(d). ϕ_G is even under time-reversal symmetry $(p_y, v, s_z) \rightarrow (-p_y, \bar{v}, \bar{s}_z)$, resulting in $T_{vs_z}(p_y) = T_{\bar{v}\bar{s}_z}(-p_y)$, which indicates that the tunneling between $|vs_z\rangle$ and $|\bar{v}\bar{s}_z\rangle$ are always symmetric, as shown in Figs. (2)(a) and (2)(b). Consequently, the transverse charge currents are always absent.

The efficiency of the charge-spin and charge-valley conversions can be characterized by the spin Hall angle (θ_S) and the valley Hall angle (θ_V), respectively, which are given by [15, 18]

$$\tan \theta_S = \frac{\sum_{vs_z} s_z \sigma_{vs_z}^\perp}{\sum_{vs_z} \sigma_{vs_z}^\parallel}, \quad \tan \theta_V = \frac{\sum_{vs_z} v \sigma_{vs_z}^\perp}{\sum_{vs_z} \sigma_{vs_z}^\parallel}. \quad (13)$$

Here the spin- and valley-dependent longitudinal conductance is given by $\sigma_{vs_z}^\parallel = (e^2/h) \sum_{p_y} T_{vs_z}$ and the transverse conductance is given by $\sigma_{vs_z}^\perp = (e^2/h) \sum_{p_y} \gamma T_{vs_z}$, where $\gamma = v_y/v_x$ is the ratio of the transverse group velocity to the longitudinal group velocity.

θ_S and θ_V versus the incident energy ϵ are shown in Fig. (3)(a). The valley Hall angle approaches the maximum value at $\epsilon \simeq 0.6$ meV with the absolute value of the valley Hall angle

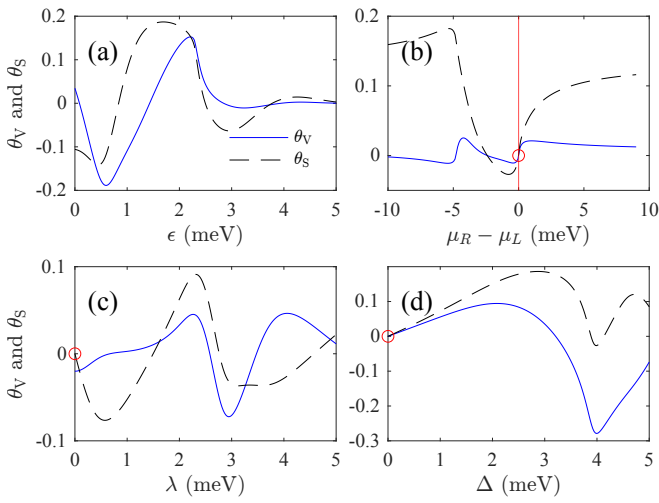


FIG. 3. (a) Spin Hall angle θ_S and valley Hall angle θ_V versus the incident energy ϵ for $\mu_L = 1$ meV, $\mu_R = -5.6$ meV. (b) Spin Hall angle θ_S and valley Hall angle θ_V versus $\mu_R - \mu_L$ for $\epsilon = 1.4$ meV. The other parameters in (a) and (b) are $\Delta = 3.25$ meV, $\lambda = 2.5$ meV, $\mu_b = 6.5$ meV and $d = 25$ nm. (c) Spin Hall angle θ_S and valley Hall angle θ_V versus λ for $\Delta = 3.25$ meV. (d) Spin Hall angle θ_S and valley Hall angle θ_V versus Δ for $\lambda = 2.5$ meV. The other parameters in (c) and (d) are $\mu_L = 1$ meV, $\mu_R = -5.6$ meV, $\mu_b = 6.5$ meV and $d = 25$ nm.

being $|\theta_V| = 0.2$. The value obtained here are comparable to that found in the tunneling valley Hall effect caused by the tilt mechanism, where $\theta_V = 0.15$ for a weak tilting Dirac cone [18]. However, the typical value of the valley Hall angle in our model is smaller than that in the pure crossed Andreev reflection assisted tunneling valley Hall effect, where the valley Hall angle can reach an order of unity [32]. For the spin Hall effect, the spin Hall angles are usually very small in semiconductors (in the range of 0.0001 to 0.001) [33, 34] but can be considerably enhanced by the single impurity scattering in graphene [4], where the spin Hall angle is in the range of 0.01 to 0.1. However, a large spin Hall angle can be generated in our model, as shown in Fig. (3)(a). θ_S approaches the maximum value at $\epsilon \approx 1.5$ meV with the maximum value being $\theta_S = 0.2$, which is comparable to the large spin Hall angle obtained in graphene grown by chemical vapour deposition [35]. θ_S and θ_V versus the difference between the left and right chemical potentials $\mu_R - \mu_L$ are shown in Fig. (3)(b). Both the TSHE and TVHE are absent at $\mu_R - \mu_L = 0$, which is attributed to the absence of the total geometric phase.

θ_S and θ_V versus the proximity-induced parameters are shown in Figs. (3)(c) and (3)(d). The pure TVHE can be generated when the spin-orbit coupling is absent, as shown in Fig. (3)(c), where $\theta_S = 0$ but a finite θ_V appears at $\lambda = 0$. This pure TVHE is attributed to the valley-contrasting geometric phase. For $\lambda = 0$, the spin-dependence of the parameter $f_{v,sz}$ is removed in Eq. (9). Swapping the valley indices results in the sign change of ϕ_G , which is responsible for the valley-contrasting skew tunneling. Both the TSHE and TVHE are

absent when the inversion symmetry is preserved in the barrier ($\Delta = 0$) due to the absence of the geometric phase, as shown in Fig. (3)(d).

The tunneling Hall effects are always associated with the momentum filtering. Compared with the existing TSHE and TVHE, the origin of the momentum filtering in our model is different. The momentum filtering in the previously proposed TSHE is attributed to the time-reversal symmetry mismatch in the tunnel junction [15–17], where the time-reversal symmetry is broken in magnetic electrodes but preserved in the nonmagnetic barrier layer with spin-orbit coupling. For the TVHE predicted in tilted Dirac and Weyl systems [18, 19], the momentum filtering occurs due to the mismatch of the Fermi surfaces of the tilted Dirac and Weyl fermions. However, the momentum filtering in our model occurs due to the transverse-momentum-dependent geometric phase shift, which is responsible for the skew coherent tunneling.

In addition, distinct from the previously proposed Berry-curvature-free TSHE and TVHE, the non- π Berry flux in the barrier region is essential in our model, which is introduced by breaking the inversion symmetry via the proximity-induced pseudospin staggered potential Δ . Furthermore, the skew tunneling occurs in the presence of a finite total backreflection geometric phase, which requires the two interfaces of the barrier to be asymmetric ($\mu_L \neq \mu_R$). This acquired total backreflection geometric phase is valley-contrasted in the absence of the spin-orbit coupling, leading to a pure TVHE, and becomes spin-dependent in the presence of the spin-orbit coupling, which is the key factor in generating the TSHE.

Conclusion.—In summary, we propose a method for the generation of the TSHE and TVHE, which is based on the phase coherent tunneling in graphene heterojunctions. In the barrier region, the pseudospin staggered potential and the intrinsic spin-orbit coupling are considered, which can be induced in graphene by the proximity effect of substrates. When the barrier of the tunnel junction has two asymmetric interfaces, the tunneling electrons acquire a finite spin- and valley-dependent geometric phase, leading to the spin- and valley-dependent skew coherent tunneling, which is responsible for the transverse spin and valley Hall currents. Distinct from the previously proposed TSHE and TVHE, this coherent-tunneling assisted Hall effect can be generated without the need for breaking time-reversal symmetry or in the absence of tilted Dirac cones, and exhibits large spin and valley Hall angles, suggesting potential applications for spintronic and valleytronic devices.

* E-mail: zeng@ujz.edu.cn

[1] I. Žutić, J. Fabian, and S. Das Sarma, Spintronics: Fundamentals and applications, *Rev. Mod. Phys.* **76**, 323 (2004).
[2] G. Wang, A. Chernikov, M. M. Glazov, T. F. Heinz, X. Marie, T. Amand, and B. Urbaszek, Colloquium: Excitons in atomically thin transition metal dichalcogenides, *Rev. Mod. Phys.* **90**, 021001 (2018).

[3] F. Pulizzi, Spintronics, *Nature materials* **11**, 367 (2012).

[4] A. Ferreira, T. G. Rappoport, M. A. Cazalilla, and A. H. Castro Neto, Extrinsic spin Hall effect induced by resonant skew scattering in graphene, *Phys. Rev. Lett.* **112**, 066601 (2014).

[5] S. Zhang, Spin Hall effect in the presence of spin diffusion, *Phys. Rev. Lett.* **85**, 393 (2000).

[6] J. Sinova, D. Culcer, Q. Niu, N. A. Sinitsyn, T. Jungwirth, and A. H. MacDonald, Universal intrinsic spin Hall effect, *Phys. Rev. Lett.* **92**, 126603 (2004).

[7] G. Y. Guo, S. Murakami, T.-W. Chen, and N. Nagaosa, Intrinsic spin Hall effect in platinum: First-principles calculations, *Phys. Rev. Lett.* **100**, 096401 (2008).

[8] J. Qi, X. Li, Q. Niu, and J. Feng, Giant and tunable valley degeneracy splitting in MoTe₂, *Phys. Rev. B* **92**, 121403 (2015).

[9] K. F. Mak, K. L. McGill, J. Park, and P. L. McEuen, The valley Hall effect in MoS₂ transistors, *Science* **344**, 1489 (2014).

[10] N. Lundt, Ł. Dusanowski, E. Sedov, P. Stepanov, M. M. Glazov, S. Klembt, M. Klaas, J. Beierlein, Y. Qin, S. Tongay, *et al.*, Optical valley Hall effect for highly valley-coherent exciton-polaritons in an atomically thin semiconductor, *Nature nanotechnology* **14**, 770 (2019).

[11] D. Xiao, W. Yao, and Q. Niu, Valley-contrasting physics in graphene: Magnetic moment and topological transport, *Phys. Rev. Lett.* **99**, 236809 (2007).

[12] M.-C. Chang and Q. Niu, Berry phase, hyperorbits, and the Hofstadter spectrum, *Phys. Rev. Lett.* **75**, 1348 (1995).

[13] D. Xiao, G.-B. Liu, W. Feng, X. Xu, and W. Yao, Coupled spin and valley physics in monolayers of MoS₂ and other group-VI dichalcogenides, *Phys. Rev. Lett.* **108**, 196802 (2012).

[14] Y. Ominato, J. Fujimoto, and M. Matsuo, Valley-dependent spin transport in monolayer transition-metal dichalcogenides, *Phys. Rev. Lett.* **124**, 166803 (2020).

[15] A. Matos-Abiague and J. Fabian, Tunneling anomalous and spin Hall effects, *Phys. Rev. Lett.* **115**, 056602 (2015).

[16] A. Vedyayev, N. Ryzhanova, N. Strelkov, and B. Dieny, Spontaneous anomalous and spin Hall effects due to spin-orbit scattering of evanescent wave functions in magnetic tunnel junctions, *Phys. Rev. Lett.* **110**, 247204 (2013).

[17] B. Scharf, A. Matos-Abiague, J. E. Han, E. M. Hankiewicz, and I. Žutić, Tunneling planar Hall effect in topological insulators: Spin valves and amplifiers, *Phys. Rev. Lett.* **117**, 166806 (2016).

[18] S.-H. Zhang, D.-F. Shao, Z.-A. Wang, J. Yang, W. Yang, and E. Y. Tsymbal, Tunneling valley Hall effect driven by tilted Dirac fermions, *Phys. Rev. Lett.* **131**, 246301 (2023).

[19] W. Zeng, Tunneling chirality Hall effect in type-I Weyl semimetals, *Phys. Rev. B* **110**, 024511 (2024).

[20] S. Zihlmann, A. W. Cummings, J. H. Garcia, M. Kedves, K. Watanabe, T. Taniguchi, C. Schönenberger, and P. Makk, Large spin relaxation anisotropy and valley-zeeman spin-orbit coupling in WSe₂/graphene/h-BN heterostructures, *Phys. Rev. B* **97**, 075434 (2018).

[21] K. Zollner and J. Fabian, Proximity effects in graphene on monolayers of transition-metal phosphorus trichalcogenides MPX₃ (M : Mn, Fe, Ni, Co, and X : S, Se), *Phys. Rev. B* **106**, 035137 (2022).

[22] Z. Khatibi and S. R. Power, Proximity spin-orbit coupling in graphene on alloyed transition metal dichalcogenides, *Phys. Rev. B* **106**, 125417 (2022).

[23] Z. Wang, D.-K. Ki, H. Chen, H. Berger, A. H. MacDonald, and A. F. Morpurgo, Strong interface-induced spin-orbit interaction in graphene on WS₂, *Nature communications* **6**, 8339 (2015).

[24] C. W. J. Beenakker, Colloquium: Andreev reflection and klein tunneling in graphene, *Rev. Mod. Phys.* **80**, 1337 (2008).

[25] Q. Cheng and Q.-F. Sun, Spin-valley-resolved energy spectra of quantum dots in the graphene/transition metal dichalcogenides system, *Phys. Rev. B* **105**, 165427 (2022).

[26] S.-C. Zhao, L. Gao, Q. Cheng, and Q.-F. Sun, Perfect crossed Andreev reflection in the proximitized graphene/superconductor/proximitized graphene junctions, *Phys. Rev. B* **108**, 134511 (2023).

[27] S. Datta, *Electronic transport in mesoscopic systems* (Cambridge university press, 1997).

[28] A. V. Shytov, M. S. Rudner, and L. S. Levitov, Klein backscattering and Fabry-Pérot interference in graphene heterojunctions, *Phys. Rev. Lett.* **101**, 156804 (2008).

[29] M. Berry, The adiabatic phase and Pancharatnam's phase for polarized light, *Journal of Modern Optics* **34**, 1401 (1987).

[30] M. Cormann, M. Remy, B. Kolaric, and Y. Caudano, Revealing geometric phases in modular and weak values with a quantum eraser, *Phys. Rev. A* **93**, 042124 (2016).

[31] S.-J. Choi, S. Park, and H.-S. Sim, Tunable geometric phase of Dirac fermions in a topological junction, *Phys. Rev. B* **87**, 165420 (2013).

[32] W. Zeng and R. Shen, Pure crossed Andreev reflection assisted transverse valley currents in $\alpha - \mathcal{T}_3$ lattices, *Phys. Rev. B* **106**, 094503 (2022).

[33] Y. K. Kato, R. C. Myers, A. C. Gossard, and D. D. Awschalom, Observation of the spin Hall effect in semiconductors, *Science* **306**, 1910 (2004).

[34] K. Ando and E. Saitoh, Observation of the inverse spin Hall effect in silicon, *Nature communications* **3**, 629 (2012).

[35] J. Balakrishnan, G. K. W. Koon, A. Avsar, Y. Ho, J. H. Lee, M. Jaiswal, S.-J. Baeck, J.-H. Ahn, A. Ferreira, M. A. Cazalilla, *et al.*, Giant spin Hall effect in graphene grown by chemical vapour deposition, *Nature communications* **5**, 4748 (2014).